Resistive Switching in Ferroelectric Bi$_2$FeCrO$_6$ Thin Films and Impact on the Photovoltaic Effect

David S. Walch, Yeseul Yun, Niranjan Ramakrishnegowda, Lutz Mühlenbein, Andriy Lotnyk, Cameliu Himcinschi, and Akash Bhatnagar*

The multiferroic character of Bi$_2$FeCrO$_6$ (BFCO), that is, the coexistence of ferroelectricity and ferromagnetism, has been predicted and demonstrated in different studies. Intriguingly, the material system also exhibits a reduced band gap, in addition to bulk-driven photovoltaic effect. The co-existence of all these attributes in a single system is a rare occurrence and paves way to a multitude of practical applications, with ferroelectric solar cell as one of them. In this work, epitaxially grown BFCO thin films, deposited with pulsed laser deposition on single crystalline SrTiO$_3$ (STO) substrates, reveal a self-ordered ionic arrangement which is proven with X-ray and transmission electron micrcoscope (TEM) measurements. A lowered band gap and a higher conductivity lead to a superior photovoltaic performance compared to a BiFeO$_3$ (BFO) reference film. Scanning probe microscopy (SPM) is used to test locally the ferroelectric switching properties. Poling with electric field not only caused a reliable change in the state of polarization, but also resulted in substantial changes in the resistance of the regions. Macroscopic measurements using transparent In$_2$O$_3$:Sn (ITO) electrodes demonstrate a bi-directional multi-stage resistive switching, which in turn influences the photovoltaic performance of the heterostucture.

D. S. Walch, Y. Yun, N. Ramakrishnegowda, L. Mühlenbein, A. Bhatnagar[+]
Zentrum für Innovationskompetenz SiLi-nano
Martin-Luther-Universität Halle-Wittenberg
06120 Halle (Saale), Germany
E-mail: akash.bhatnagar@physik.uni-halle.de
D. S. Walch, Y. Yun, N. Ramakrishnegowda, L. Mühlenbein, A. Bhatnagar
Institut für Physik
Martin-Luther-Universität Halle-Wittenberg
06120 Halle (Saale), Germany
A. Lotnyk
IOM Leibniz-Institut für Oberflächenmodifizierung
04318 Leipzig, Germany
C. Himcinschi
TU Bergakademie Freiberg
Institut für Theoretische Physik
09596 Freiberg, Germany

The ORCID identification number(s) for the author(s) of this article can be found under https://doi.org/10.1002/aelm.202200276.

[+]Present address: SCHOTT AG Hattenbergstraße 10, 55122 Mainz, Germany

1. Introduction

Magnetoelectric multiferroics, that is, materials exhibiting a rare combination of ferroelectricity and ferromagnetism, are of great interest for the development of new-age functional materials.[1–3] Especially, if the coexistence of the two ferroic orders manifests via a strong coupling, the materials can be used for ferroelectric data storage devices with magnetic readout. Bi$_2$FeCrO$_6$ (BFCO) has been theoretically predicted as one of the most promising candidate in this context, with a large spontaneous polarization and magnetization.[4,5] The multiferroic character has been confirmed experimentally in epitaxial BFCO thin films.[6–8]

Beyond, an anomalous photovoltaic effect, also known as bulk photovoltaic (BPV) effect, is relevant for crystals lacking inversion symmetry, and thus also for all ferroelectrics.[9–12] The BPV effect depends on the light polarization state and the orientation of the ferroelectric polarization.[13–15] Subsequent experiments on the optical properties of BFCO thin films indeed unraveled a photovoltaic effect which was found to be sensitive to the orientation of the ferroelectric polarization.[16–18] Interestingly, the effective band gap may be adjusted by tuning the ionic ordering within the film[19,20] and thus the development of a multilayer BFCO device achieved a solar conversion efficiency of 8.1% under AM1.5 illumination, the highest reported from a ferroelectric until now.[21] A necessary precondition was the application of a high electric field in order to align the ferroelectric polarization uniformly in one direction. However, the application of electric fields may influence the electrical resistance as reported in Au/BFCO/LaNiO$_3$/SiO$_2$/Si heterostructure[22] and in BFCO/SRO/STO thin films.[23]

The coexistence of multiferroic, photovoltaic, and resistive switching properties makes BFCO an ideal material to conceptualize novel (self-powered) photo-neuromorphic devices, for example, combining photovoltaic and neuromorphic applications.[24] In conjunction, the response to light essentially also allows non-destructive readout of both, resistive and ferroelectric, state of the material.[25]

In this work, BFCO thin films on STO (001) single-crystalline substrates with either SrRuO$_3$ (SRO) or La$_{0.7}$Sr$_{0.3}$MnO$_3$ (LSMO) as intermediate conductive layer were fabricated using pulsed laser deposition (PLD). The quality of the films was

characterized using X-ray diffraction, SPM and TEM measurements. The superior photovoltaic performance of BFCO was first established upon comparison with BFO, as the short-circuit current density (i_{sc}) from BFCO exceeded that of BFO by around 700 times. The ferroelectric behavior was demonstrated and visualized with piezoresponse force microscopy (PFM) while the resistive states were observed with conductive atomic force microscopy (C-AFM). Sequential poling of regions assisted in ruling-out the polarization-flip as the underlying origin for the observed resistive switching effect. Macroscopic measurements were conducted that unraveled a case of bidirectional multi-stage resistive switching. The use of ITO as top electrodes facilitated the photovoltaic measurements on the same device, and enabled analyzing the corresponding impact. The variations in the conductance were sufficient to induce a change in the resultant open-circuit voltage (V_{oc}), an evident footprint of bulk-driven photovoltaic effect. The results further highlight the utility of light as a tool for read-out purposes.

2. Results and Discussion

BFCO thin films with a thickness of around 100 nm were deposited on single-crystalline STO (001) substrates using a PLD system. Details on the thin film growth can be found in the Experimental Section. Conductive SRO or LSMO buffer layers were deposited to enable (photo) electrical measurement across the BFCO thin film (see inset **Figure 1a**). Crystallinity and phase purity of the heterostructures were confirmed with X-ray measurement. The resultant $2\theta - \omega$ scans around the (002) substrate peak are presented in Figure 1a. Additionally,

high-resolution TEM images of the BFCO/SRO//STO structure can be found in Figure S1, Supporting Information. In case of BFCO/SRO//STO (red), the peaks arising from BFCO and SRO appear to be merged together as both layers grow under compressive epitaxial strain and exhibit similar lattice parameter. On the other hand, in case of BFCO/LSMO//STO (blue), the larger lattice constant of STO compared to LSMO results in tensile epitaxial strain, and consequently the peaks from LSMO and BFCO are split from one another separated by the STO substrate peak. Reciprocal space maps (RSM) around the (204) STO plane for both samples are shown in Figure 1b. In particular, the RSM of the BFCO/LSMO//STO shows two distinct peaks arising from the BFCO layer. The BFCO split-peak is also visible in BFCO/SRO//STO, although, not distinguishable into two. The closeness with the lattice parameter of SRO results in a rather convoluted four-way split.

One possible reason for this observation is the existence of a layered structure within the BFCO film, evidently visible in the cross-sectional images acquired with TEM in Figure 1c. Further analysis conducted with energy dispersive X-rays (EDX) mapping provided a qualitative proof of the existence of Fe- and Cr-rich regions across the entire thickness of the sample (see EDX profiles in Figure S2, Supporting Information). While in some regions the dominant presence of one and the depletion of the other ion is clearly visible. As expected, the A-site cation, Bi^{3+}, is found to be uniformly distributed. However, local analysis of d-spacing using TEM in BFCO layer at different regions did not show any significant changes. The existence of different domain variants (with different in-plane polarization direction) can cause a layer peak splitting in the RSM measurements which has been known in BFO[26] and also recently
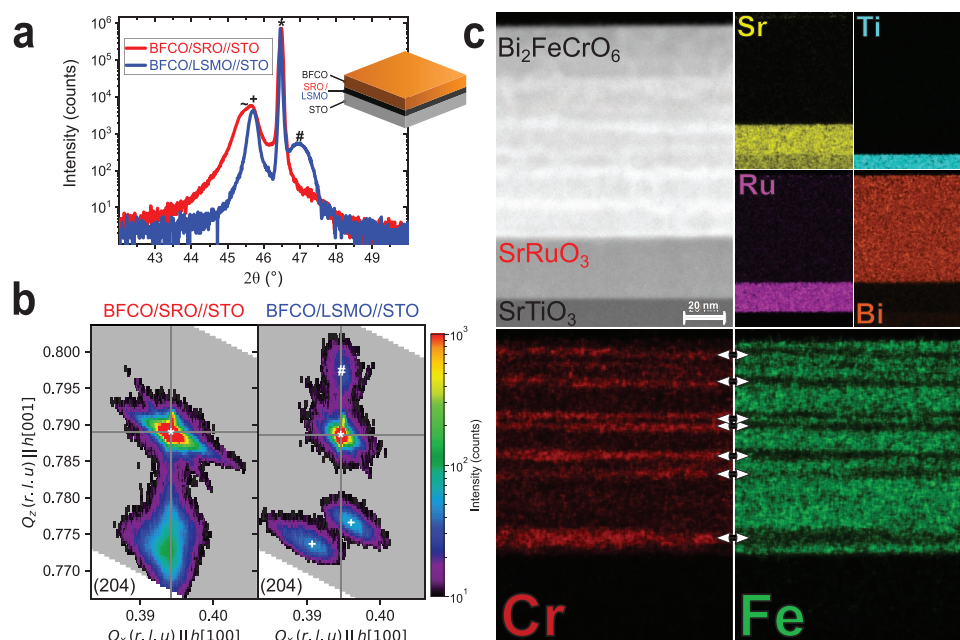
Figure 1. Structural characterization. a) $2\theta - \omega$ scans around (002) substrate peak of BFCO/SRO//STO (red) and BFCO/LSMO//STO (blue) films (* STO substrate, $^+$ BFCO, $^\#$ LSMO, $^\sim$ SRO). b) RSM maps around (204) substrate plane of BFCO/SRO//STO (left) and BFCO/LSMO//STO (right) film. c) STEM-HAADF image (top left). EDX maps of Sr (yellow), Ti (turquoise), Ru (pink), Bi (orange) (all top right), Cr (red, bottom left), and Fe (green, bottom right).
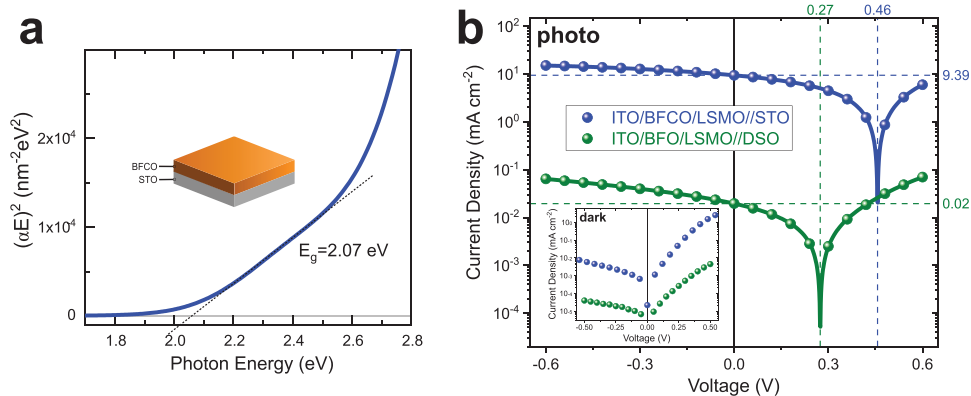
Figure 2. Initial photovoltaic measurements. a) The square of the product between absorption coefficient α and the energy *E*, as function of energy of a BFCO//STO structure. The bandgap was determined by the linear extrapolation to zero absorption. b) Current– voltage characteristics under 405 nm illumination of ITO/BFCO/LSMO//STO (blue) and ITO/BFO/LSMO//DSO structure (green). Fit (solid lines) used to extract V_{oc} values.

demonstrated in BFCO thin films.[27] In other recent publications, such peak-split was attributed to existence of cationic ordered and disordered domains within the BFCO layers.[17,21,28]

2.1. Photovoltaic Effect

The ordering of the iron and chromium ions at the B-sites, studied with ab initio calculations by Baettig et al., results in rather intricate hybridizations between the 3d orbitals of iron and chromium with the oxygen 2p orbital.[4,5] Interestingly, the chromium 3d states do not only contribute to the conduction band but their hybridization with oxygen 2p orbital is also not negligible and plays host to spin-polarized holes. An evident impact is on the photovoltaic properties which have been found to be much improved in comparison to any other ferroelectric.[20,21]

We validated this scenario by measuring the ellipsometry spectra of the BFCO//STO structure. From the BFCO extinction coefficient determined by ellipsometry, the absorption coefficient α was calculated. The onset of absorption region was analyzed and a bandgap of ≈2.07 eV was obtained by linear extrapolation of $(\alpha E)^2$ versus energy as it is shown in **Figure 2**a. This value is significantly lower than the reported direct bandgaps of BFO (2.7 eV)[29,30] or BCO (2.95 eV)[31] thin films. The determined value of band gap is in good agreement with literature values determined for BFCO films, and it can be tuned by the growth conditions.[21,32–34] Lowering of bandgap values has also been observed in other Fe/Cr mixed systems in comparison with the parent compounds (as in the case of $LaFe_{0.5}Cr_{0.5}O_3$[35] or $HoFe_{0.5}Cr_{0.5}O_3$[36]) due to charge transfer excitation between Fe and Cr.
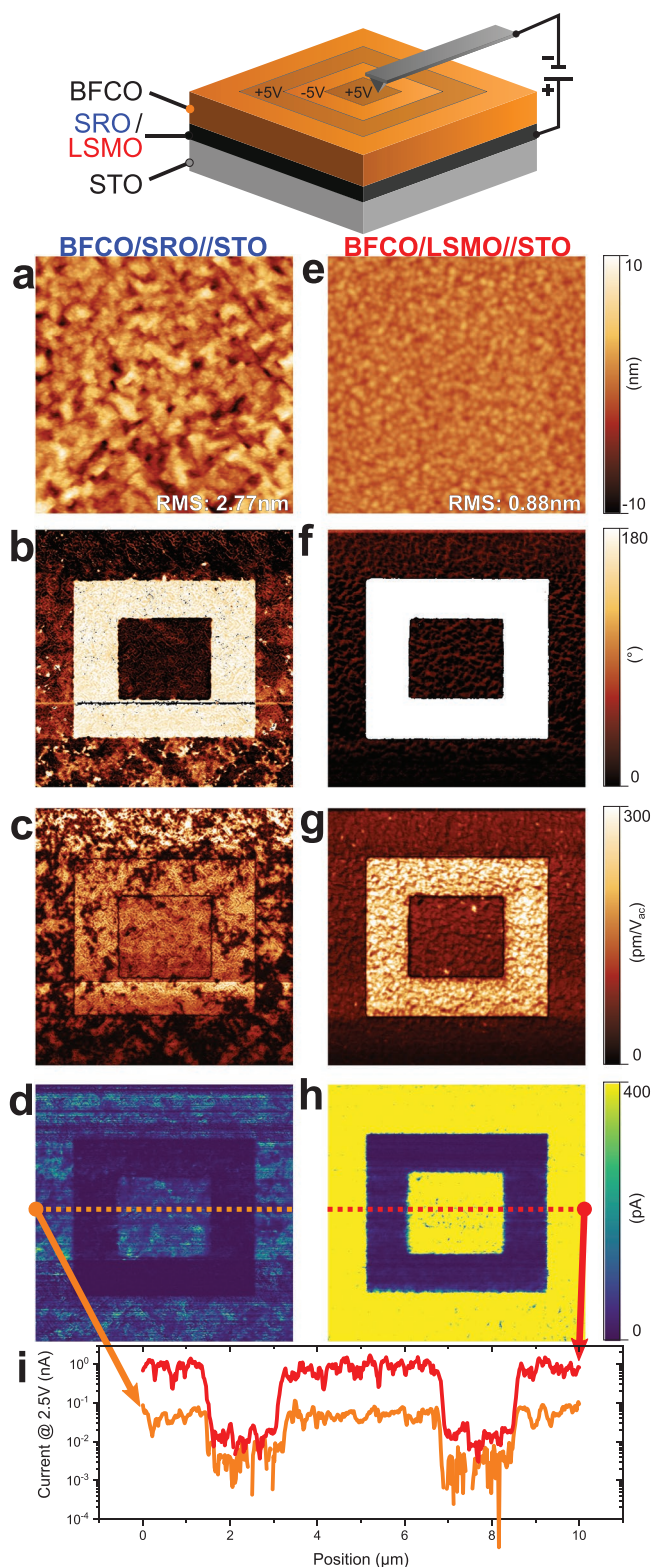
To measure the photovoltaic properties, electrodes were structured using a photolithography process and subsequently ITO was deposited on the BFCO/LSMO//STO structure using a radio frequency sputtering machine (see Experimental Section). BFCO/LSMO//STO structure was used for macroscopic measurements primarily for three reasons: i) extent or nature of ordering in the BFCO samples if one considers the RSM in Figure 1b; ii) reduced surface roughness (see **Figure 3**a,e), thus the interface between top electrode and the surface can

be expected to be more homogeneous and; iii) homogeneous response from ferroelectric domains in PFM measurements (see Figure 3b,f). Figure 2b shows the resultant current– voltage (*I–V*) characteristics under laser light illumination (3.06 eV, 405 nm) that reveal a V_{oc} of 0.46 V and an i_{sc} of 9.39 mA cm^{-2}, which culminates into a higher photovoltaic performance if compared with a ITO/BFO/LSMO//DSO reference sample (V_{oc} = 0.27 V, i_{sc} = 0.02 mA cm^{-2}). The dark *I–V* (inset) also demonstrates a higher conductivity of the BFCO/LSMO//STO structure compared to the BFO reference film. Under solar simulator illumination (1.5 AM), the photovoltaic performance of the ITO/BFCO/LSMO//STO structure reduces to V_{oc} = 0.21 V and i_{sc} = 73.1 µA cm^{-2} (see Figure S3, Supporting Information). This is still much lower compared to the highly efficient single layer BFCO thin films reported by Nechache et al.,[21] however, the application of high electric fields prior to the photovoltaic measurement is needed to align the ferroelectric polarization uniformly in one direction.

2.2. Scanning Probe Microscopy

PFM measurements were performed to verify the switchability and retention of polarization. DC voltages of opposite polarity were applied subsequently in squared-regions of diminishing sizes that is, +5 V: 10 × 10 µm² → −5 V : 6 × 6 µm² → +5 V : 3 × 3 µm², (see schematic Figure 3 top). The consequent vertical PFM measurements are shown in Figure 3a–c,e–g for the BFCO/SRO//STO and BFCO/LSMO//STO films, respectively. The topography of the BFCO/LSMO//STO film (Figure 3e) reveals a reduced roughness and grain size compared to the BFCO/SRO//STO film (Figure 3a). Importantly, the topographies remain unchanged after the application of the DC voltages. For both the samples, the contrast in the vertical PFM phase images (Figure 3b,f), corresponding to the oppositely-poled regions, clearly confirms ferroelectric switching. The vertical PFM amplitude images reveal the domain walls separating the written domains (Figure 3c,g).

To gain further information on the resistive/conductive state, C-AFM measurements were performed subsequently on the same area. The resulting current maps (Figure 3d,h)

**ADVANCED
SCIENCE NEWS**

www.advancedsciencenews.com

**ADVANCED
ELECTRONIC
MATERIALS**

www.advelectronicmat.de

Figure 3. Scanning probe microscopy. Topography, vertical PFM phase, vertical PFM amplitude, C-AFM (read-out voltage 2.5 V) images (10 × 10 μm²) for BFCO/SRO//STO (a–d) and BFCO/LSMO//STO (e–h), respectively, with corresponding current line profiles (i).
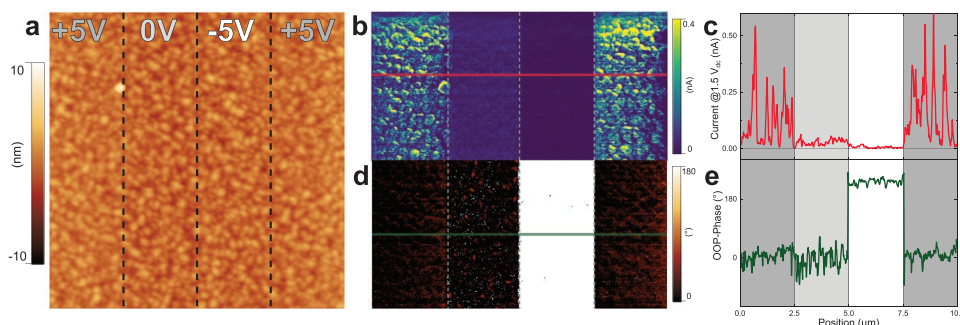
show also a contrast, which is more pronounced with higher currents for the BFCO/LSMO//STO film as emphasized in the line scans in Figure 3i. The contrasts clearly suggest the formation and persistence of states exhibiting different values of resistance. Although such resistive switching behavior has been demonstrated with C-AFM on BFCO/Nb:STO films,[34] the fields needed to pole the samples were much larger (+9 V) despite nearly half the thickness (49 nm). Furthermore, measurements on ultrathin (6 nm) BFCO films on SRO-buffered STO have demonstrated the coexistence of ferroelectric and bipolar resistive switching, also under the C-AFM tip.[23]

Additionally, systematic scans were conducted with SPM to evaluate the correlation between the observed ferroelectric and resistive switching. The AFM topography image in **Figure 4**a shows the outline of a subdivided area into four equally large rectangular parts (each 2.5 × 10 μm²). Different voltages (+5 V, 0 V, −5 V, +5 V) were applied to each area. The subsequent C-AFM (only upper half shown) and PFM (only lower half shown) measurements with corresponding line scan are shown in Figures 4b,c and 4d,e, respectively. The C-AFM image (readout voltage 1.5 V) shows only a high current response in +5 V-poled areas with maximum currents exceeding 500 pA. The measured current at the pristine (0 V) and −5 V-poled area is much lower with maximum current values in the range of tens of picoamperes. The current of the right half of the C-AFM current map (−5 V, 5 V) mimics the findings presented in Figures 3 and 5, in which the material is in the high-resistive (HR) and low-resistive (LR) state after the applications of positive and negative voltages, respectively. Importantly, despite the fact that the ferroelectric polarization within the +5 V-poled and pristine area are alike, as apparent from the vertical PFM phase images, the CFM images clearly suggests a much different state of resistance in the two regions. This essentially demonstrates the coexistence of ferroelectric and resistive switching, while being independent from one another.

2.3. Macroscopic Electrical Measurements

Upon observation of switchable ferroelectric and resistive states using SPM techniques, $I–V$ characteristics of the BFCO/LSMO//STO sample were measured with a larger voltage range and ITO as the top electrode. The current measured during a triangular voltage sweep (0 V → +5 V→ −5 V→ 0 V) at a rate of 0.1 V s^{-1} is shown in **Figure 5**a. In the positive voltage regime, a splitting of forward and backward scan is observed. With opposite polarity, the splitting becomes even more evident with distinct turning point at about −2 V. Focusing on the slope of the curve around the origin, a relatively higher slope can be observed after the application of positive voltages than after negative.

To get a deeper insight, the measurement was repeated, albeit, with acquisition of intermediate $I–V$ characteristics. After every 0.5 V, $I–V$ characteristics with a smaller voltage range of ±0.2 V (see Figure 5b inset) was acquired to gain information on the resistive/conductive state of the sample. The resultant intermediate $I–V$ curves always exhibit linear

**ADVANCED
SCIENCE NEWS**

www.advancedsciencenews.com

**ADVANCED
ELECTRONIC
MATERIALS**

www.advelectronicmat.de

Figure 4. Comparing initial, HR, and LR states using SPM measurements. a) AFM image (10×10 μm^2) with dotted lines indicating areas of different applied voltages. b,c) C-A FM current map of the upper half and corresponding line scan (read-out voltage 1.5 V). d,e) Vertical PFM phase images of lower half and corresponding line scan.
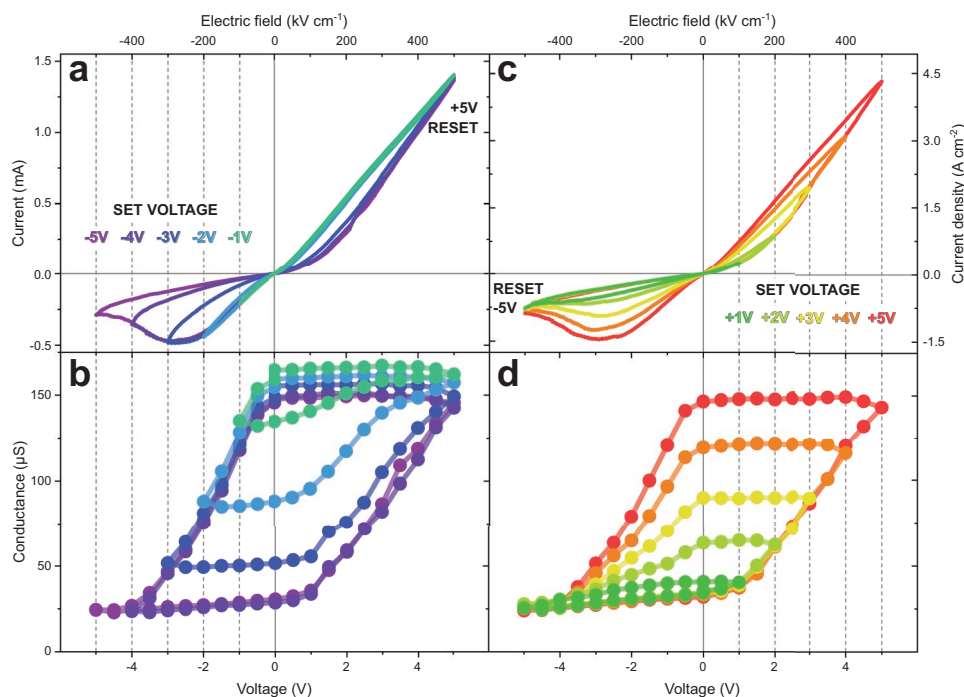
characteristic, and the extracted slope is sufficient to estimate the conductance and is plotted as a function of the applied voltage. The conductance as a function of applied voltage is shown in Figure 5b reveals a hysteretic behavior, in which the LR and HR state is obtained after application of positive and negative voltages, respectively. Such hysteretic behavior of the gap conductance has been observed in ferroelectric tunnel junctions, however, with only a several nanometer thick ferroelectric BaTiO$_3$ layer.[37–40] The linear current response within
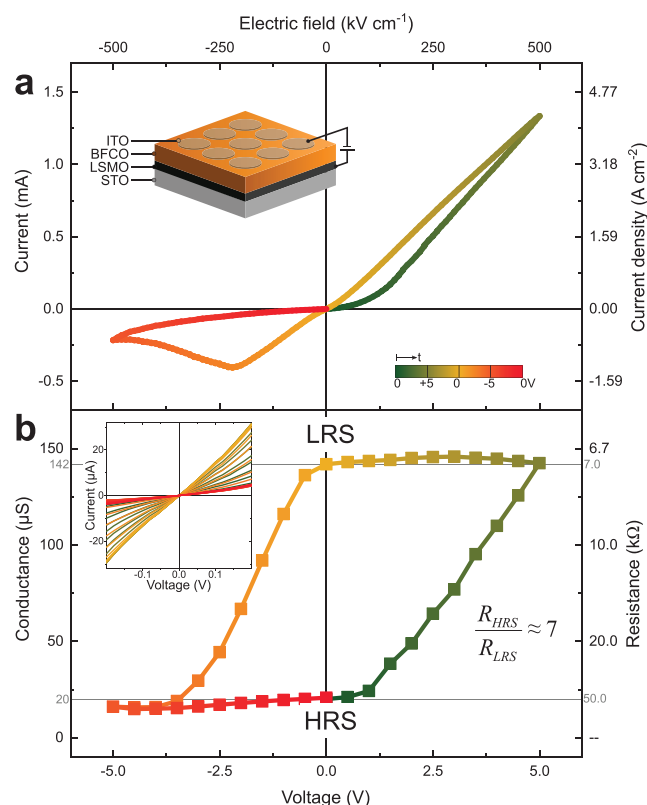
the narrow voltage range of the sample essentially also rules out the role of ferroelectric polarization-related mechanisms which have been widely reported to result in diode-like *I–V* characteristics.[41–43] These aspects were further verified with dielectric measurements wherein the typical features associated with polarization-switching were not observed in capacitance–voltage measurements (see Figure S4, Supporting Information).

The hysteretic character of the switching behavior can be utilized to deterministically set different resistive states. This aspect has been presented in **Figure 6**a,b that shows with current–voltage and corresponding conductance–voltage characteristics, respectively with asymmetric voltage range and opposed sweeping direction. The measurements were conducted in two separate cycles. In the first cycle, the reset voltage was fixed at +5 V and individual *I–V* curves were measured as the set voltage was step-wise varied from −5 to −1 V with a step size of 1 V. The results clearly demonstrated the impact of the applied electric field on the conductance of the material, as the differences in the conductance (between HRS and LRS) and the effective resistance may be tuned from about 50 to 7 kΩ, respectively. The lower is the magnitude of the set voltage, the higher the resulting conductance ranging from the HR toward LR state at the end of the half-cycle. Note, the repeated application of a high reset voltage while lowering of set voltage magnitude results in a slight overall increase of the conductance at the end of the final cycles. As shown in Figure 5b the conductance hysteresis is not completely symmetric. In the positive voltage regime, the conductance does not seem to be saturated contrary to the negative direction. In the second cycle, the measurements were repeated, albeit with reset voltage as −5 V and set voltage varied from +5 to +1 V. The conductance after applying the set voltages reduces from the LRS toward the HRS with decreasing values of set voltage. The conductance saturates at about −4 V. Therefore and in contrast to Figure 5b, a continuing decrement of the conductance after repeated application of the negative reset voltage is not observed and the conductance after resetting is constant in Figure 5d. Figure 6 demonstrates the possibility of bi-directional multistage resistive switching in the ITO/BFCO/LSMO//STO heterostructure.

Figure 5. Resistive switching in macroscopic measurement. a) Current–voltage characteristic with schematic of ITO/BFCO/LSMO//STO structure. b) Hysteretic conductance–voltage behavior extracted from small range current–voltage characteristics (inset).

2200276 (5 of 9)

Figure 6. Multistage bi-directional resistive switching. Current–voltage and conductance–voltage characteristics with reducing set voltage magnitude in a,b) negative direction and c,d) positive direction, respectively.

Recent publications also demonstrated resistive switching in Au/BFCO/LaNiO$_3$/SiO$_2$//Si[22] and Au/BFCO/SnO$_2$:F[44] structures attributing the effect to changed boundary condition due to oxygen vacancy migration toward the interfaces.
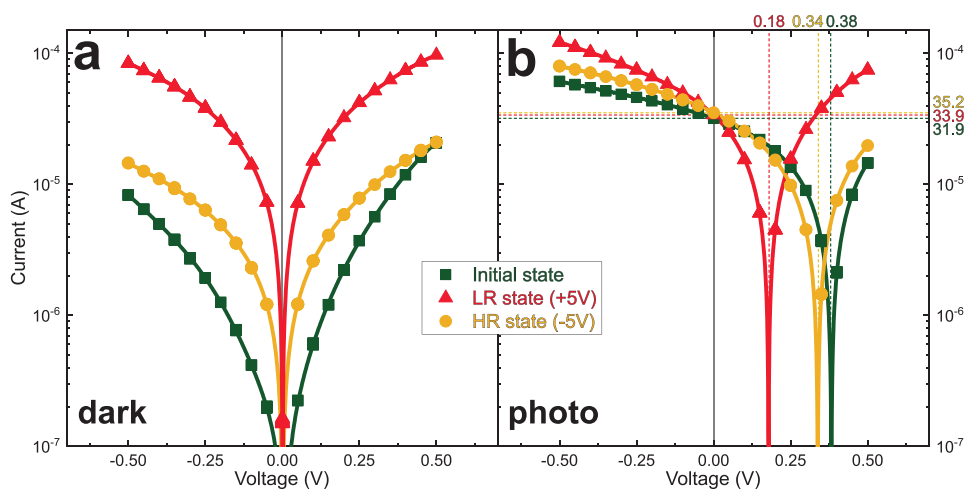
2.4. Influence of Resistive Switching on Photovoltaic Effect

Figure 7a shows the dark I–V characteristics for the pristine, LR and HR states. The HR state has slightly higher conductivity than the pristine state, while the LR state exhibits much larger

conductivity resulting in high currents under bias fields. An increased dark conductivity influences the photovoltaic effect under the assumption that the charge-separation mechanism proceeds via bulk photovoltaic effect, which can be described by the following equation

$$V_{oc} = -\frac{I_{sc}l}{A(\sigma_{ph} + \sigma_{dark})} \tag{1}$$

Where l, A, σ_{ph}, and σ_{dark} are the distance between the electrodes, the area, the photo and dark conductivity, respectively.

Figure 7. Influence of resistive switching on photovoltaic properties/optical sensing of resistive state. a) Dark and b) photo (405 nm laser illumination) current–voltage characteristics of initial, LR, and HR state. Fit (solid lines) used to extract V_{oc} values.

In case of constant I_{sc}, the resultant V_{oc} depends on the overall conductivity of the material. Hence, the LR and HR states may be used to tune the obtainable V_{oc} from the devices.

Figure 7b presents I–V characteristics acquired under laser light with photon energy of 3.06 eV. Interestingly, the short-circuit current (I_{sc}) from each state, that is, HR state (-35.2 µA), LR state (-33.9 µA), and initial state (-35.2 µA) remain largely similar. However, there is a apparent change in the corresponding V_{oc}. It changes from 0.38 V in the initial state, to 0.18 V in the LR state, and back to 0.34 V in the HR state. Similar to the situation in Figure 7a, the V_{oc} does not completely recover back to the pristine state. Comparing HR and LR state, the V_{oc} and resistance (under light) reduce by half (V_{oc}: factor $V_{oc,HR}/V_{oc,LR} \approx 0.53$; $R_{HR}/R_{LR} = 10.61$ kΩ/5.75 kΩ ≈ 0.54) according to Equation (1).

Alternatively, Figure 7b also demonstrates the possibility to use the photovoltaic effect to read out the conductive/resistive state of the material. Similar findings have been shown in ITO/BaTiO$_3$/LSMO//STO ferroelectric tunnel junctions at low temperature, in which the resulting V_{oc} depends on the resistive state of the memristor.[39,40]

3. Conclusions

Epitaxial BFCO-based heterostructures were fabricated and were tested for their photoelectric, ferroelectric, and resistive switching properties. X-ray analysis was conclusive in proving the single crystalline nature of the samples and RSM suggested partial ordering of Fe and Cr ions at the B-site. TEM measurements confirmed the existence of Fe- and Cr-rich layers throughout the film thickness and atomic EDX provided a visual proof. In line with theoretical calculations, the ordering at the B-site not only serves lowering the band gap, but may also have an impact on the resultant conductivity.[4] Consequently, the photoresponse from the BFCO was measured to be around 700 times larger than from BFO. SPM techniques, that is PFM and C-AFM, were used to test investigate the surface and ferroelectric properties. The polarization was switchable with ±5 V and written domains remained stable. In the C-AFM mode, the domains of opposite polarities exhibited massively different states of electrical resistance with differences of more than one order of magnitude. Systematic scans conducted with different bias voltages, suggested little or no interlink between the ferroelectric and resistive states of the samples. Hence it can be implied, that oxygen ion migration and related mechanisms might be at the origin of the observed effects. Another aspect worthy to be mentioned is the higher conductivity in BFCO in comparison to BFO (inset Figure 2b) which in turn also results in much larger currents during the resistive switching. A possible reason could be the lower binding of oxygen 1s orbital in the BFCO in comparison to BFO, allowing the oxygen ions to easily dissociate.[45]

Macro-scale measurements were conducted to further analyze the resistive switching characteristics. The SET and RESET voltages were successfully implemented to fine-tune the conductive states of the sample, and switch between HR, LR, and intermediate states. The absence of any abrupt change in the conductivity further supports this argument

and suggests a rather homogeneous migration of oxygen-ions during the SET and RESET processes.[46] The observed gradual changes in the resistance, also referred to as analogue switching, are prerequisite for the realization of neuromorphic devices.[47] The possibility to tune the conductance was eventually utilized to tune the V_{oc} under light which also evidently suggests the dominance of bulk-driven photoeffects in the samples. It is imperative to note here that the direction of I_{sc}, and corresponding polarity of V_{oc}, remain unchanged after the application of SET/RESET voltages, thereby ruling out any role of ferroelectric switching. The synergistic overlap of the different functionalities elaborated in this work namely, ferroelectricity, resistive switching and photovoltaics, presents BFCO as a rather lucrative system for highly coveted self-powered photo-neuromorphic applications.

4. Experimental Section

Thin Film Growth Using Pulsed Laser Deposition and Electrode Fabrication: The heterostructures were grown on single-crystalline STO (001)$_c$ substrates using a pulsed laser deposition system (SURFACE PLD-Workstation, KrF excimer laser). The distance between the stoichiometric ceramic targets and the substrate is set to 60 mm. The films were cooled down at a rate of 20 °C min^{-1} under a oxygen partial pressure of ≈200 mbar (**Table 1**).

Top electrodes were structured using a direct-write photolithography machine (DMO MicroWriter ML3) and ITO as transparent, conductive electrode materials (thickness 100–125 nm) were subsequently evaporated using a RF sputtering machine.

Spectroscopic Ellipsometry: The ellipsometric measurements were performed by using a M2000 J.A. Woollam ellipsometer. The ellipsometric data were evaluated and from the determined optical constants of BFCO the absorption coefficient α was calculated.

Transmission Electron Microscopy: Cross-sectional specimen for TEM investigations was prepared by focused gallium ion beam milling (Zeiss Auriga Dual-beam FIB). A probe Cs-corrected Titan3 G2 60-300 microscope was used for TEM studies. The microscope was operated at 300 kV accelerating voltage. The Titan was equipped with high-brightness gun (X-FEG), several annual detectors (Fischione, FEI), and Super-X energy-dispersive X-ray spectroscopy (EDS) system (FEI ChemiSTEM technology). Probe-forming aperture of 20 mrad was used during scanning TEM (STEM) measurements. STEM images were recorded with an annular dark-field detector (Fischione) using annular ranges of 80–200 mrad, which correspond to high-angle annular dark-field (HAADF) imaging condition. EDX maps were recorded in STEM mode using the Super-X EDS system. The maps were acquired and processed with Bruker software. The beam currents were set to 150 pA during the EDX mapping.

Scanning Probe Microscopy: SPM measurements were acquired with a Asylum Research Cypher equipped with a platinum-coated tip (MikroMasch NSC 15). PFM measurements were performed in Dual AC Resonance-Tracking (DART) mode with AC voltage of 1.5–2.5 V and a center drive frequency of ≈1.3 MHz. For C-AFM measurements, the read-out voltage was set to values of 1.5–2.5 V.

Table 1. PLD deposition parameters.

	BFCO	SRO	LSMO	BFO
Substrate temperature [°C]	700	750	650	725
O$_2$ partial pressure [mbar]	0.01–0.02	0.067	0.2	0.145
Laser repetition rate [Hz]	1–2	1	2	2
Laser fluence [J cm^{-2}]	1.50	1.16	1.33	1.50

**ADVANCED
SCIENCE NEWS**

www.advancedsciencenews.com

**ADVANCED
ELECTRONIC
MATERIALS**

www.advelectronicmat.de

(Photo) Electrical Measurements: A high impedance electrometer / source meter (Keithley 6517B / Keithley 2450) acted as a voltage source (*I–V* characteristics, switching voltage) and simultaneously measured the current. The samples were illuminated by a diode laser (Cobolt 06 MLD / Thorlabs LDM9T) with a wavelength of 405 nm and 20 mW power. Additionally, a diode-based solar simulator (Wavelabs SINUS-70) was used as a light source to measure under 1.5 AM condition.

Conflict of Interest

The authors declare no conflict of interest.

Author Contributions

A.B. and D.S.W. designed and conceived the experiments. D.S.W. was responsible for thin film growth, PFM analysis, and (photo) electric measurements. Y.Y., N.R., and L.M. participated in structural characterization. TEM specimen preparation and measurements were conducted by A.L. C.H. performed ellipsometric measurements and analysis. A.B. and D.S.W. co-wrote the manuscript with inputs from all the co-authors.

Data Availability Statement

The data that support the findings of this study are available from the corresponding author upon reasonable request.

[1] N. A. Hill, *J. Phys. Chem. B* **2000**, *104*, 6694.

[2] N. A. Hill, A. Filippetti, *J. Magn. Magn. Mater.* **2002**, *242-245*, 976.

[3] W. Eerenstein, N. D. Mathur, J. F. Scott, *Nature* **2006**, *442*, 759.

[4] P. Baettig, C. Ederer, N. A. Spaldin, *Phys. Rev. B* **2005**, *72*, 2111.

[5] P. Baettig, N. A. Spaldin, *Appl. Phys. Lett.* **2005**, *86*, 012505.

[6] R. Nechache, C. Harnagea, A. Pignolet, F. Normandin, T. Veres, L. P. Carignan, D. Ménard, *Appl. Phys. Lett.* **2006**, *89*, 102902.

[7] R. Nechache, P. Gupta, C. Harnagea, A. Pignolet, *Appl. Phys. Lett.* **2007**, *91*, 222908.

[8] R. Nechache, L. P. Carignan, L. Gunawan, C. Harnagea, G. A. Botton, D. Ménard, A. Pignolet, *J. Mater. Res.* **2007**, *22*, 2102.

[9] V. M. Fridkin, B. N. Popov, *Sov. Phys.-Usp.* **1978**, *21*, 981.

[10] V. I. Belinicher, I. F. Kanaev, V. K. Malinovsky, B. I. Sturman, *Ferroelectrics* **1978**, *22*, 647.

[11] B. I. Sturman, V. M. Fridkin, *The Photovoltaic and Photorefractive Effects in Noncentrosymmetric Materials*, Gordon and Breach, Philadelphia **1992**.

[12] V. M. Fridkin, *Crystallogr. Rep.* **2001**, *46*, 654.

[13] A. Bhatnagar, A. Roy Chaudhuri, Y. Heon Kim, D. Hesse, M. Alexe, *Nat. Commun.* **2013**, *4*, 2835.

[14] D. S. Knoche, Y. Yun, N. Ramakrishnegowda, L. Mühlenbein, X. Li, A. Bhatnagar, *Sci. Rep.* **2019**, *9*, 13979.

[15] D. S. Knoche, M. Steimecke, Y. Yun, L. Mühlenbein, A. Bhatnagar, *Nat. Commun.* **2021**, *12*, 282.

[16] R. Nechache, C. Harnagea, S. Licoccia, E. Traversa, A. Ruediger, A. Pignolet, F. Rosei, *Appl. Phys. Lett.* **2011**, *98*, 202902.

[17] W. Huang, C. Harnagea, D. Benetti, M. Chaker, F. Rosei, R. Nechache, *J. Mater. Chem. A* **2017**, *5*, 10355.

[18] W. Huang, J. Chakrabartty, C. Harnagea, D. Gedamu, I. Ka, M. Chaker, F. Rosei, R. Nechache, *ACS Appl. Mater. Interfaces* **2018**, *10*, 12790.

[19] S. Zhang, H. Y. Xiao, S. M. Peng, G. X. Yang, Z. J. Liu, X. T. Zu, S. Li, D. J. Singh, L. W. Martin, L. Qiao, *Phys. Rev. Appl.* **2018**, *10*, 044004.

[20] L. Wei, C. Li, X. Li, J. Guo, D. Ge, L. Guan, B. Liu, *Appl. Phys. Express* **2019**, *6*, 096112.

[21] R. Nechache, C. Harnagea, S. Li, L. Cardenas, W. Huang, J. Chakrabartty, F. Rosei, *Nat. Photonics* **2015**, *9*, 61.

[22] H. L. Zhou, Y. P. Jiang, X. G. Tang, Q. X. Liu, W. H. Li, Z. H. Tang, *ACS Appl. Mater. Interfaces* **2020**, *12*, 54168.

[23] W. Xu, J. Sun, X. Xu, G. Yuan, Y. Zhang, J. Liu, Z. Liu, *Appl. Phys. Lett.* **2016**, *109*, 152903.

[24] A. Pérez-Tomás, *Adv. Mater. Interfaces* **2019**, *6*, 1900471.

[25] R. Guo, L. You, Y. Zhou, Z. S. Lim, X. Zou, L. Chen, R. Ramesh, J. Wang, *Nat. Commun.* **2013**, *4*, 1990.

[26] Y. H. Chu, M. P. Cruz, C. H. Yang, L. W. Martin, P. L. Yang, J. X. Zhang, K. Lee, P. Yu, L. Q. Chen, R. Ramesh, *Adv. Mater.* **2007**, *19*, 2662.

[27] Y. Liu, J. Lin, N. Zhong, P. H. Xiang, Y. Chen, P. Yang, J. Chu, C. G. Duan, L. Sun, *J. Appl. Phys.* **2020**, *128*, 234103.

[28] W. Huang, C. Harnagea, X. Tong, D. Benetti, S. Sun, M. Chaker, F. Rosei, R. Nechache, *ACS Appl. Mater. Interfaces* **2019**, *11*, 13185.

[29] S. R. Basu, L. W. Martin, Y. H. Chu, M. Gajek, R. Ramesh, R. C. Rai, X. Xu, J. L. Musfeldt, *Appl. Phys. Lett.* **2008**, *92*, 091905.

[30] D. Sando, C. Carrétéro, M. N. Grisolia, A. Barthélémy, V. Nagarajan, M. Bibes, *Adv. Optical Mater.* **2018**, *6*, 1700836.

[31] C. Himcinschi, I. Vrejoiu, T. Weißbach, K. Vijayanandhini, A. Talkenberger, C. Röder, S. Bahmann, D. R. T. Zahn, A. A. Belik, D. Rafaja, J. Kortus, *J. Appl. Phys.* **2011**, *110*, 073501.

[32] S. Li, B. AlOtaibi, W. Huang, Z. Mi, N. Serpone, R. Nechache, F. Rosei, *Small* **2015**, *11*, 4018.

[33] A. Quattropani, D. Stoeffler, T. Fix, G. Schmerber, M. Lenertz, G. Versini, J. L. Rehspringer, A. Slaoui, A. Dinia, S. Colis, *J. Phys. Chem. C* **2018**, *122*, 1070.

[34] M. V. Rastei, F. Gellé, G. Schmerber, A. Quattropani, T. Fix, A. Dinia, A. Slaoui, S. Colis, *ACS Appl. Energy Mater.* **2019**, *2*, 8550.

[35] J. Andreasson, J. Holmlund, S. G. Singer, C. S. Knee, R. Rauer, B. Schulz, M. Käll, M. Rübhausen, S. G. Eriksson, L. Börjesson, A. Lichtenstein, *Phys. Rev. B* **2009**, *80*, 075103.

[36] G. Kotnana, S. N. Jammalamadaka, *J. Appl. Phys.* **2015**, *118*, 124101.

[37] H. J. Mao, C. Song, L. R. Xiao, S. Gao, B. Cui, J. J. Peng, F. Li, F. Pan, *Phys. Chem. Chem. Phys.* **2015**, *17*, 10146.

[38] J. Li, C. Ge, J. Du, C. Wang, G. Yang, K. Jin, *Adv. Mater.* **2020**, *32*, 1905764.

[39] A. Rivera-Calzada, F. Gallego, Y. Kalcheim, P. Salev, J. Del Valle, I. Tenreiro, C. León, J. Santamaría, I. K. Schuller, *Adv. Electron. Mater.* **2021**, *7*, 2100069.

[40] I. Tenreiro, V. Rouco, G. Sánchez-Santolino, F. Gallego, C. Leon, A. Rivera-Calzada, I. K. Schuller, J. Santamaria, *Appl. Phys. Lett.* **2022**, *120*, 034101.

[41] T. Choi, S. Lee, Y. J. Choi, V. Kiryukhin, S. W. Cheong, *Science* **2009**, *324*, 63.

[42] C. Wang, K. j. Jin, Z. t. Xu, Le Wang, C. Ge, H. b. Lu, H. z. Guo, M. He, G. z. Yang, *Appl. Phys. Lett.* **2011**, *98*, 192901.

[43] S. Hong, T. Choi, J. H. Jeon, Y. Kim, H. Lee, H. Y. Joo, I. Hwang, J. S. Kim, S. O. Kang, S. V. Kalinin, B. H. Park, *Adv. Mater.* **2013**, *25*, 2339.

[44] S. Hu, Z. Tang, L. Zhang, D. Yao, Z. Liu, S. Zeng, X. Guo, Y. Jiang, X. G. Tang, L. Ma, Z. Nie, J. Gao, *J. Mater. Chem. C* **2021**, *9*, 13755.

[45] R. Nechache, C. Harnagea, L. P. Carignan, D. Ménard, A. Pignolet, *Philos. Mag. Lett.* **2007**, *87*, 231.

[46] S. Slesazeck, T. Mikolajick, *Nanotechnology* **2019**, *30*, 352003.

[47] W. Zhang, B. Gao, J. Tang, X. Li, W. Wu, H. Qian, H. Wu, *Phys. Status Solidi RRL* **2019**, *13*, 1900204.